nature COMMUNICATIONS

ARTICLE

https://doi.org/10.1038/s41467-022-29102-0 OPEN

Selective photocatalytic CO_2 reduction in aerobic environment by microporous Pd-porphyrin-based polymers coated hollow TiO_2

Yajuan Ma[1], Xiaoxuan Yi[1], Shaolei Wang[2], Tao Li[1], Bien Tan[1], Chuncheng Chen[3], Tetsuro Majima[1], Eric R. Waclawik[4], Huaiyong Zhu[4] & Jingyu Wang[1]✉

Direct photocatalytic CO_2 reduction from primary sources, such as flue gas and air, into fuels, is highly desired, but the thermodynamically favored O_2 reduction almost completely impedes this process. Herein, we report on the efficacy of a composite photocatalyst prepared by hyper-crosslinking porphyrin-based polymers on hollow TiO_2 surface and subsequent coordinating with Pd(II). Such composite exhibits high resistance against O_2 inhibition, leading to 12% conversion yield of CO_2 from air after 2-h UV-visible light irradiation. In contrast, the CO_2 reduction over Pd/TiO_2 without the polymer is severely inhibited by the presence of O_2 (≥ 0.2 %). This study presents a feasible strategy, building Pd(II) sites into CO_2-adsorptive polymers on hollow TiO_2 surface, for realizing CO_2 reduction with H_2O in an aerobic environment by the high CO_2/O_2 adsorption selectivity of polymers and efficient charge separation for CO_2 reduction and H_2O oxidation on Pd(II) sites and hollow TiO_2, respectively.

---

[1] Key Laboratory of Material Chemistry for Energy Conversion and Storage (Ministry of Education), School of Chemistry and Chemical Engineering, Huazhong University of Science and Technology, Wuhan 430074, China. [2] Key Laboratory of Polyoxometalate Science of Education Institution, Faculty of Chemistry, Northeast Normal University, Changchun 130024, China. [3] Key Laboratory of Photochemistry, CAS Research/Education Center for Excellence in Molecular Sciences, Institute of Chemistry, Chinese Academy of Sciences, Beijing 100190, China. [4] School of Chemistry, Physics and Mechanical Engineering, Queensland University of Technology, Brisbane QLD 4001, Australia. ✉email: wangjingyu@hust.edu.cn

Photocatalytic CO_2 reduction into useful fuels is a promising approach to tackle the challenges of carbon emission and global warming by directly utilizing sustainable solar energy[1–3]. Despite extensive efforts and many attempts at harnessing various semiconductor photocatalysts for CO_2 reduction, most of the photocatalytic reactions occur only at high CO_2 concentration and sometimes CO_2-philic organic solvents are required to make them operate efficiently, due to low CO_2 uptake of the photocatalysts[1–6]. Physisorptive microporous solids such as microporous organic polymers and metal-organic frameworks have recently emerged as promising candidates to replace aqueous amines for CO_2 capture and storage[7–11]. Several reports demonstrated the integration of metals into CO_2-adsorptive materials could convert diluted CO_2 due to the high CO_2 uptake and high reduction activity of metals during the photocatalytic reactions[12–14]. However, metal sites suffer from poor H_2O oxidation activity and highly active for H_2 evolution from H_2O, so that these photocatalysts require addition of Ru-containing photosensitizer together with organic sacrificial reagent and solvent[12–14], which present unsustainable and negative environmental impact issues. More importantly, anaerobic environment is essential to avoid the competitive reaction of oxygen reduction because it is thermodynamically favored compared to CO_2 reduction[15–20].

An ideal catalyst is capable of taking gaseous feedstocks[21]. In practice, the CO_2 concentration in air is as low as 300~400 ppm, and flue gas after fossil fuel combustion typically consists of about 72–77 vol% N_2, 12–14 vol% CO_2, 8–10 vol% H_2O, 3–5 vol% O_2, and other minor components[21–24]. In air and flue gas, the CO_2 adsorption and activation on the surface of photocatalysts are low, due to the competitive O_2 adsorption and reduction, as well as the low CO_2 concentration[15–20]. Catalytic CO_2 reduction is strongly influenced by the presence of 5 ppm of O_2 and completely inhibited in 5 vol% O_2, because O_2 reduction is thermodynamically favored compared to CO_2 reduction[20]. Therefore, to control CO_2 emission from exhaust gas and reduce CO_2 concentration in air, developing efficient photocatalysts with selective CO_2 adsorption and conversion in an aerobic environment remains a challenge.

To address the challenge, we envisioned that significantly increasing CO_2 concentration around the catalytic active sites for CO_2 reduction via preferential adsorption of CO_2 over O_2 could lessen the inhibitive impact of O_2 and promoting H_2O oxidation could increase CO_2 conversion. High CO_2 adsorption capability and selectivity of microporous polymers with heterocyclic skeleton and large π-conjugated structure can bring opportunities for directly using low concentration of CO_2 without separation from aerobic mixtures if the catalytic active sites for CO_2 reduction are built in the polymer. For the photocatalytic CO_2 reduction with H_2O in such an aerobic environment, another essential requirement is to assemble the photocatalytic sites for CO_2 reduction and H_2O oxidation for efficient separation of photogenerated electrons and holes, respectively. Meanwhile, H_2O provides protons for reacting with the intermediates from CO_2 reduction, increasing CH_4 production. Electron transfer at the heterointerface between two components is required for the occurrence of CO_2 reduction and H_2O oxidation at different active sites in a composite structure.

In this work, a proof-of-concept study was conducted to verify this hypothesis. We prepared a porous composite photocatalyst by in situ hyper-crosslinking porphyrin-based polymers (HPP) on a hollow TiO_2 surface, followed by loading Pd(II) via coordination with HPP to form the CO_2 reduction sites (Pd-HPP-TiO_2). Hollow TiO_2 was used to increase the heterointerface between TiO_2 and Pd-HPP. The choice of Pd allows us to confirm the influence of CO_2 adsorption and charge separation on the reduction. The heteroatom-rich microporous structure can not only improve the capability and selectivity of CO_2 adsorption in an aerobic environment but also stabilize Pd(II) sites, while anatase TiO_2 surface is highly efficient for H_2O oxidation with holes that generated in the valence band from the bandgap excitation. Pd-HPP-TiO_2 achieves the efficient conversion of CO_2 in an aerobic environment, i.e., 12 % of CO_2 in air is converted after 2-h UV-visible light irradiation with a CH_4 production of 24.3 μmol g^{-1}, which is 4.5 times higher than that over Pd/TiO_2. Based on the catalytic activity, we identify the active sites for photocatalytic CO_2 reduction and discuss the overall reaction mechanism.

Results and discussion

Preparation of porous Pd-HPP-TiO_2. The synthetic processes of porous Pd-HPP-TiO_2 are depicted in Fig. 1. HPP were knitted

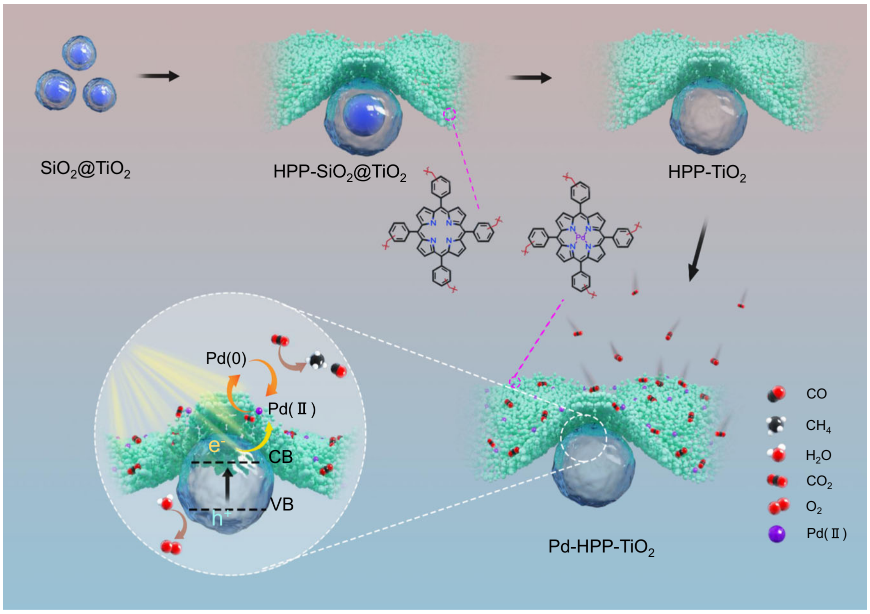

Fig. 1 Schematic illustrations. Synthesis of porous Pd-HPP-TiO_2 and the possible mechanism of photocatalytic CO_2 reduction. The chemical structures of HPP and Pd-HPP units are provided.

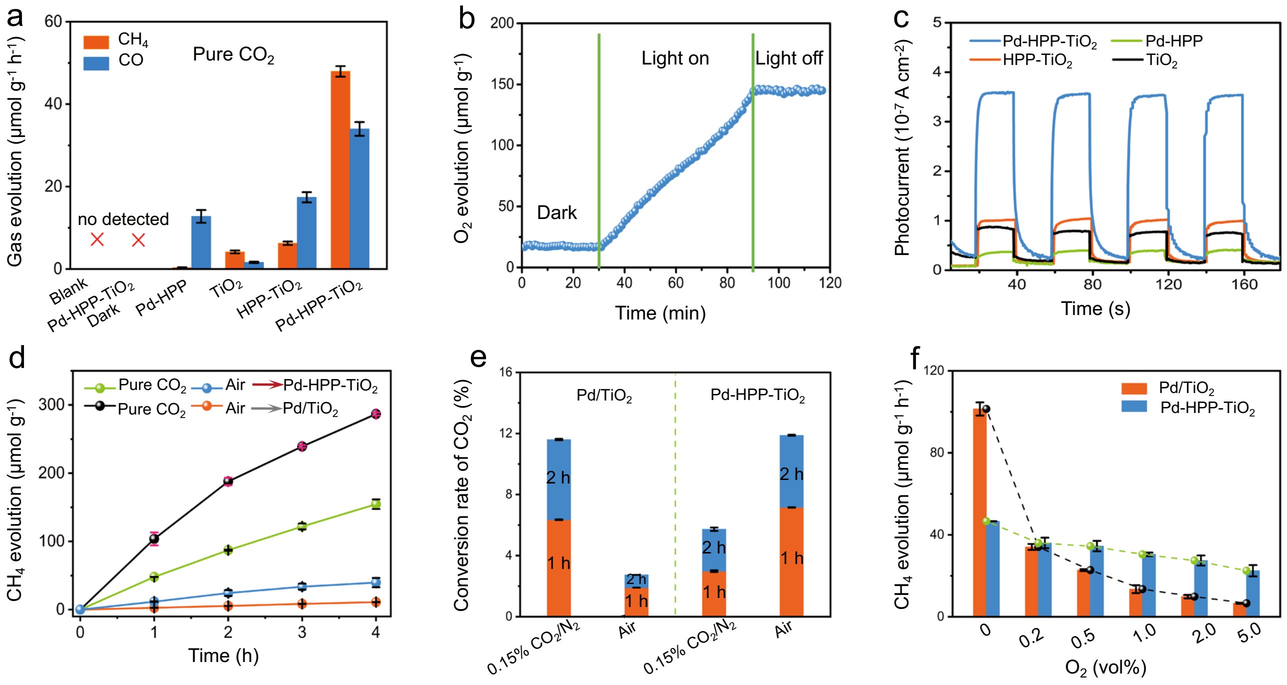

Fig. 2 Evaluation of photocatalytic CO_2 reduction. **a** The evolution rates of CH_4 and CO in pure CO_2. **b** On-line monitoring of O_2 evolution during the photocatalytic reaction over Pd-HPP-TiO_2. **c** Photocurrent response during light on-off cycling. **d** Comparison of the CH_4 evolution rates in pure CO_2 and air. **e** The conversion yield of CO_2 by measuring the CO_2 concentration. **f** Effect of O_2 concentration (vol%) in CO_2/O_2 gas mixture on the CH_4 evolution rate. The results in (**a**, **d**, **e**, **f**) are the average values of three parallel experiments. The error bar represents the standard deviation of the measurements.

together from 5,10,15,20-tetraphenylporphyrin (TPP) building blocks on the surface of core-shell $SiO_2@TiO_2$ with the diameter of 100–150 nm used as solid templates. The SiO_2 cores were then etched by NaOH solution to produce hollow TiO_2 with the thickness of about 10 nm coated by layers of HPP with the thickness of about 5–7 nm (HPP-TiO_2), finally Pd(II) coordinates with the core of porphyrin unit, leading to the formation of porous Pd-HPP-TiO_2 (details are provided in the Methods). The photocatalytic activity was evaluated in a gas-solid reaction without the addition of photosensitizer or organic sacrificial reagent under UV-visible light irradiation. CH_4 and CO were detected as the main products, in accordance with the results from many gas-solid reactions[25,26]. To clarify the effect of HPP, Pd/TiO_2 was synthesized as a control by photo-deposition of Pd nanoparticles on the surface of hollow TiO_2.

Photocatalytic CO_2 reduction. Figure 2a shows the comparison of CH_4 and CO evolution rates over a series of photocatalysts in pure CO_2. Hollow TiO_2 presented evolution rates of 4.2 and 1.6 μmol g^{-1} h^{-1} for CH_4 and CO, respectively. HPP-TiO_2 caused a moderate increase of CO evolution rate, mainly arising from the introduction of an abundance of micropores on HPP, favoring the CO_2 uptake. When building Pd(II) sites into HPP-TiO_2, the CO_2 reduction efficiency was further enhanced, reaching high evolution rates of 48.0 and 34.0 μmol g^{-1} h^{-1} (average value within 4 h) for CH_4 and CO, respectively. The comparison to the reported results under similar reaction conditions suggests the excellent photocatalytic activity of porous Pd-HPP-TiO_2 composite (Supplementary Table 1). The high selectivity as 59% for CH_4 production over Pd-HPP-TiO_2 can be attributed to the Pd(II) sites with sufficient energy overcoming the Schottky barrier with TiO_2 and improving the charge separation efficiency[27]. In a long-term test, Pd-HPP-TiO_2 showed continuous CH_4 and CO production up to 20 h under UV-visible light irradiation (Supplementary Fig. 1). Although there is somewhat loss in catalytic activity, the superior performance of porous Pd-HPP-TiO_2 to Pd/TiO_2 during long-term photocatalytic reaction suggests that the introduction of microporous HPP greatly contributes to stabilizing Pd(II) sites. No detectable H_2 during the photocatalytic reaction suggests the higher CO_2 reduction selectivity than H_2O reduction. It is noted that Pd-HPP exhibits the ability to catalyze the conversion of CO_2 to CO, which is consistent with the reports on various metal complexes[12–14,28]. Only CH_4 was produced over the photocatalysts containing TiO_2. The surface of anatase TiO_2 efficiently adsorbs H_2O to facilitate H_2O oxidation and provide protons for the CO_2 reduction to yield CH_4[29–31]. The efficient consumption of light-generated holes on the TiO_2 surface can accelerate the overall reaction.

The photocatalytic CO_2 reduction was confirmed by a series of control experiments, (1) dark reaction, (2) without photocatalyst, (3) in N_2, and (4) isotopic label using $^{13}CO_2$. No detectable product in the dark or the absence of photocatalysts indicates that the CO_2 reduction proceeded as a light driven catalytic process (Fig. 2a). Upon replacing CO_2 with N_2, trace amounts of CH_4 and CO were detected after the photocatalytic reaction (Supplementary Fig. 2), presumably due to the slight decomposition of HPP and the presence of pre-adsorbed CO_2 on the photocatalyst or reactor surface. Isotopically labeled $^{13}CO_2$ (^{13}C enrichment of ≥ 97%) was used as the reactant to study the origin of products. According to the ion fragment analysis, the peaks at 2.5 min and 7.2 min in the gas chromatography could be assigned to CH_4 and CO, respectively. As compared to the signals of products under $^{12}CO_2$, the appearance of ion fragment peaks at $m/z = 17$ and 29 reveals that the produced $^{13}CH_4$ and ^{13}CO originated from $^{13}CO_2$ reduction over Pd-HPP-TiO_2 (Supplementary Fig. 3). The overall reaction involves CO_2 reduction and H_2O oxidation cycles to produce CH_4, CO, and O_2, respectively, but their concentration changes in the whole cycle have seldom been measured in the literature[32]. The in-situ monitoring of O_2 evolution during the photocatalytic reaction was performed to further verify the CO_2 reduction by H_2O (Fig. 2b). When the experiment was conducted in the dark, low O_2 concentration in the reaction remained unchanged and came from the residual air, which was not completely removed by the degassing procedure. By way of contrast, during the photocatalytic reaction, the concentration of O_2 increased linearly with an evolution rate of 127 μmol g^{-1} h^{-1}. Thus, the electrons (e^-) being provided from the 4-e^- oxidation are comparable to the total electrons for CH_4 and CO production via 8-e^- and 2-e^- reduction processes. When UV-visible light irradiation was turned off, the O_2 concentration remained constant. This result illustrates that CO_2 is reduced by H_2O during photocatalytic reaction over Pd-HPP-TiO_2 and that the backward reaction does not take place.

As for the photocatalytic CO_2 reduction, the reaction involved several steps, light absorption to generate electrons and holes in TiO_2, electron transfer from the conduction band of TiO_2 to Pd-HPP, electron trapping at the catalytic Pd(II) sites in Pd-HPP, reduction of the adsorbed CO_2 on Pd(II) sites[33]. The charge separation and charge transfer efficiency were investigated by electrochemical, photochemical, and photoelectrochemical measurements. The hollow TiO_2 displays a large semicircle arc at the high frequency of electrochemical impedance spectrum (EIS), indicating less electronic conductivity and larger electron transfer resistance (R_{ct}) (Supplementary Fig. 4). The value of R_{ct} in the EIS of HPP-TiO_2 is smaller than those of both TiO_2 and Pd-HPP, indicating that the interface between the polymer and TiO_2 facilitates the electron transfer. The smallest value of R_{ct} in the EIS of Pd-HPP-TiO_2 illustrates the efficient interfacial electron transfer by the surface binding HPP coordinating with Pd on hollow TiO_2. When coating with Pd-HPP, the photoluminescence of TiO_2 was almost quenched, indicating the efficient suppression of photogenerated charge recombination through radiative pathways (Supplementary Fig. 5). The photogenerated electrons are expected to transfer from the photoexcited TiO_2 to Pd(II) sites in HPP, leading to effective separation of electrons from the holes left in TiO_2. In addition, the introduction of Pd enhanced the interaction with gas molecules such as O_2 and CO_2 from air, which also causes the quenching of photoluminescence on TiO_2 surface[34–36]. Similar results for Pd/TiO_2 to Pd-HPP-TiO_2 in Supplementary Figs. 4 and 5 reveal that Pd in Pd-HPP contributes to the efficient charge separation. The amperometric signals provide further information on the relative efficiency of the electron transfer in the materials under UV-visible light irradiation. The electronic conductivity of Pd-HPP appears to be higher than TiO_2, and Pd-HPP exhibits the lowest photocurrent among the samples (Fig. 2c). Generally, the photoinduced charge separation in organic polymers does not occur dominantly as compared with exciton migration, leading to the lower capability as redox photocatalysts[37]. Although Pd-HPP possesses strong absorption in the visible region (Supplementary Fig. 6), both Pd-HPP and Pd-HPP-TiO_2 exhibit low photocatalytic activity for CO_2 reduction under visible light irradiation, suggesting the low efficiency of charge separation in HPP (Supplementary Fig. 7). It is found that such results are comparable to the recently reported analogous polymer photocatalyst[38]. The comparison of visible light driven CO_2 reduction to that under UV-visible light is presented in Supplementary Fig. 8. Thus, the photocatalytic CO_2 reduction reaction over Pd-HPP-TiO_2 depended on UV light of UV-visible light irradiation. The visible light is absorbed by HPP, and most of photons absorbed are changed to heat. When TiO_2 is irradiated with UV light to generate electrons and holes in conduction band and valence band, respectively, the electrons transfer at the heterointerface to HPP with π-conjugated structure and can be trapped at Pd(II). It is well know that metals work as electron trap sites to enhance the charge separation efficiency[39]. The highest photocurrent of Pd-HPP-TiO_2 can be attributed to the photogenerated electrons transferring from TiO_2 to Pd-HPP and to be trapped at Pd. The order of gas evolution rates shown in Fig. 2a is consistent with that of the photocurrent in Fig. 2c, suggesting that efficient electron transfer in Pd-HPP is the dominant influence on the photocatalytic activity with pure CO_2.

Pd in Pd-HPP increases the charge separation efficiency, while Pd does not response to the selective CO_2 reduction in an aerobic environment. In pure CO_2, Pd/TiO_2 exhibits high activity for CH_4 production with a rate of 104 μmol g^{-1} h^{-1} compared to Pd-HPP-TiO_2 (48.0 μmol g^{-1} h^{-1}), as shown in Fig. 2d. In the case of similar Pd loading, the higher rate over Pd/TiO_2 is ascribed to Pd-HPP absorbing light in a part (Supplementary Fig. 6) and thus decreasing absorbed photon numbers by TiO_2. Besides, the light-induced electron transfer from TiO_2 to Pd in Pd/TiO_2 is more efficient compared with that in Pd-HPP-TiO_2, in which Pd sites do not directly contact with hollow TiO_2. When the reaction proceeded in diluted CO_2 (diluted in N_2), the CH_4 evolution rate over Pd/TiO_2 was higher than that over Pd-HPP-TiO_2 (Supplementary Fig. 9a), but the difference between them was less with decreasing the CO_2 concentration (Supplementary Fig. 9b), due to the enrichment of low CO_2 concentration by the abundant micropores of HPP. The activities for two photocatalysts were close each other using the synthetic gas containing 0.03 vol% CO_2 (approximate concentration of air, Supplementary Fig. 9b). However, in air, the CO_2 reduction was almost completely inhibited over Pd/TiO_2, while it still proceeded over Pd-HPP-TiO_2 with the evolution rates of 12.2 μmol g^{-1} h^{-1} and 4.9 μmol g^{-1} h^{-1} for CH_4 and CO production, respectively (Fig. 2d and Supplementary Table 2). The calculated conversion yields of CO_2 over two catalysts in air and a mixture of CO_2 and N_2 are compared in Fig. 2e. Monitoring of change in CO_2 concentration is important in providing direct evidence for the CO_2 conversion, but it has been seldom achieved in the literatures because the change is negligibly little in pure CO_2. It is noted that the reduction efficiency in the gas mixture of 0.15 vol% CO_2 in N_2 is close to that in pure CO_2, and the change in CO_2 concentration is large enough to calculate the conversion yield, as listed in Supplementary Table 3. Pd/TiO_2 is more efficient than Pd-HPP-TiO_2 in an anaerobic environment, while the reverse results were observed in air; CO_2 conversion yields of 12% and 2.7% over Pd-HPP-TiO_2 and Pd/TiO_2, respectively, after 2 h UV-visible light irradiation. The yield of 12% is the highest among the CO_2 conversions in air reported in the literatures (Supplementary Table 2). The difference between the CO_2 conversion yields in 0.15 vol% CO_2 in N_2 and air is resulted from the absence and presence of O_2, respectively. Thus, we investigated the effect of O_2 concentration on the photocatalytic reaction. As can be seen in Fig. 2f, for Pd/TiO_2, the presence of 0.2 vol% O_2 suppressed the CH_4 evolution rate, and the presence of 5 vol% O_2 dropped it steeply to 6% of that in pure CO_2[5]. Interestingly, the negative effect of O_2 on the CH_4 evolution is significantly less over Pd-HPP-TiO_2: the presence of 5 vol% O_2 decreased it to 46% of that in pure CO_2.

Porosity and gas uptake. For heterogeneous catalysis, the reaction rate is usually proportional to the surface coverage of reactants on the catalyst, so the CO_2 conversion efficiency particularly relies on the CO_2 adsorption on the photocatalysts[33,40,41]. The surface properties including porosity as well as the CO_2 adsorption capability and selectivity of as-prepared samples were investigated. As shown in Fig. 3a, the N_2 adsorption-desorption isotherms of Pd-HPP and Pd-HPP-TiO_2 exhibit a steep increase at relative low pressure ($P/P_0 < 0.001$) and an obvious hysteresis at medium pressure, which indicate the existence of abundant micropores and mesopores[42]. This

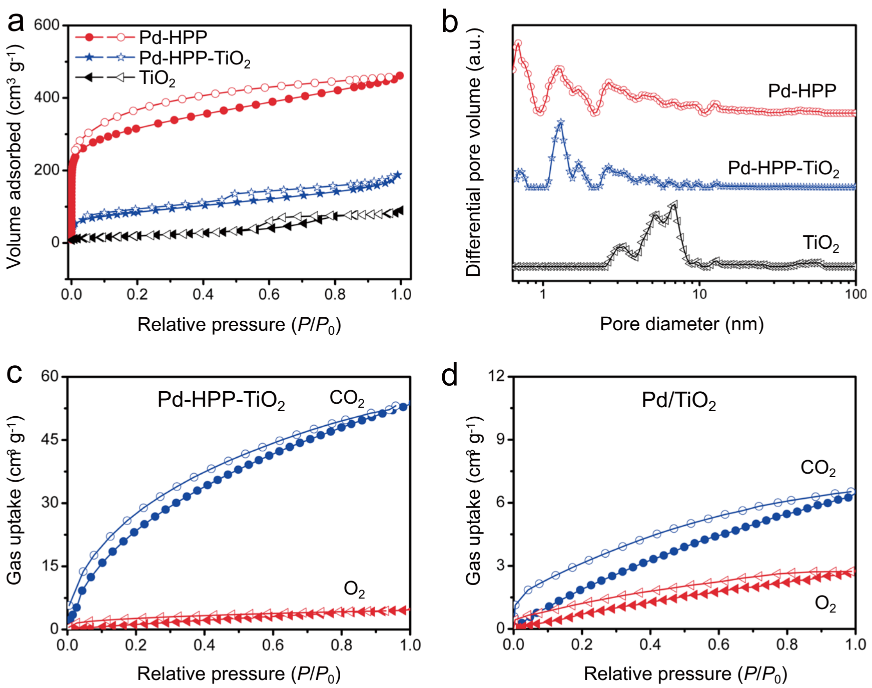

Fig. 3 Surface porosity and gas uptake. (**a**) N_2 adsorption-desorption isotherms and (**b**) pore size distribution plots of hollow TiO_2, Pd-HPP, and Pd-HPP-TiO_2. Comparisons in CO_2 and O_2 uptake of (**c**) Pd-HPP-TiO_2 and (**d**) Pd/TiO_2 at 273 K.

result may be due to a fast rate of hyper-crosslinking and the low degree of free packing for building blocks by Friedel-Crafts alkylation reaction. In contrast, pure hollow TiO_2 shows the character of type IV isotherm with a hysteresis loop at medium pressure, which suggests the formation of mesoporous structure and gives a Brunauer–Emmett–Teller surface area (S_{BET}) of 75 $m^2\ g^{-1}$. Owing to the high microporosity of HPP (0.7 and 1.3 nm), Pd-HPP-TiO_2 has a large surface area of 323 $m^2\ g^{-1}$ and micropore volume of 0.22 $cm^3\ g^{-1}$ (Supplementary Table 4). The introduction of TiO_2 caused a moderate decrease of the ultra-micropore of HPP, while micropores centered at 1.3 nm were largely remained (Fig. 3b). The microporous nature of Pd-HPP-TiO_2 causes the CO_2 enrichment around the catalytic active Pd sites in Pd-HPP. The CO_2 adsorption capability of Pd-HPP-TiO_2 reaches as high as 54.0 $cm^3\ g^{-1}$ at 1.0 bar and 273 K, which is 4.9 times higher than that of TiO_2 (Fig. 3c and Supplementary Fig. 10). In contrast, the as-obtained Pd/TiO_2 shows a low CO_2 uptake of 6.5 $cm^3\ g^{-1}$ under similar conditions. To study the effect of porphyrin concentration on the adsorption of CO_2 and photocatalytic reaction, we have prepared porous Pd-HPP-TiO_2 composites with different mass percentage of porphyrin unit by adjusting the adding amount of porphyrin monomer. The CO_2 uptake of porous Pd-HPP-TiO_2 composites with 53.8 and 74.9 wt% of Pd-HPP was presented in Supplementary Fig. 11. According to the adding amount of porphyrin monomer and the yield of resulted polymer, the mass percentage of porphyrin unit in Pd-HPP is calculated to be about 70.5%. Thus the molar ratios of porphyrin unit/adsorbed CO_2 can be calculated and compared in Supplementary Table 5. The results suggest that the ratio of porphyrin/CO_2 almost keeps constant. A little lower porphyrin/CO_2 ratio in Pd-HPP-TiO_2 composites than that in pure Pd-HPP is presumably due to the introduction of TiO_2 slightly blocking the crosslinking of porphyrin monomer. It can be concluded that the adsorption of CO_2 molecules strongly depends on the porphyrin content. Besides the CO_2 adsorption, electron generation on TiO_2 photocatalyst and trapping by Pd(II) sites are crucial processes that involved in the photocatalytic reactions. The result of photocatalytic CO_2 reduction in Supplementary Fig. 12 reveals that there is an appropriate porphyrin content that balanced the CO_2 adsorption and conversion efficiency.

The selectivity ratio of CO_2/O_2 over Pd/TiO_2 is 3.1 calculated by initial slopes of adsorption isotherms in the low pressure region (Fig. 3d and Supplementary Fig. 13), indicating a mediocre CO_2 adsorption selectivity in the presence of O_2. Interestingly, Pd-HPP-TiO_2 exhibits a high CO_2/O_2 selectivity ratio of 23.9. Moreover, CO_2 has delocalized π-bonds with higher quadrupole moment (-13.4×10^{-40} C m^2) than O_2 (-1.03×10^{-40} C m^2)[43,44]. Introducing porphyrin with a core of four pyrrole rings as the building blocks into microporous materials endows them polarizing N-containing groups and large π-conjugated structure, which could response to the enhanced interaction with CO_2[9–11,45]. The high affinity for CO_2 instead of O_2 for microporous Pd-HPP-TiO_2 is consistent with the selective CO_2 adsorption and reduction. Thus the photocatalytic CO_2 reduction is achieved in an aerobic environment by taking the advantage of selective CO_2 adsorption in microporous HPP.

Structural analysis. Structural characterizations provide more information for understanding the selective CO_2 adsorption and conversion. Pd-HPP-TiO_2 displays the X-ray diffraction (XRD) peaks of pure TiO_2 anatase (Fig. 4a). No diffraction peak of Pd crystal indicates Pd (II) coordinates to the porphyrin in Pd-HPP. The observation by scanning electron microscopy (SEM) reveals the morphology of the core-shell SiO_2@TiO_2 to have a uniform size of 100~200 nm for template-assisted knitting of TPP (Supplementary Fig. 14). The transmission electron microscopy (TEM) and high-resolution TEM (HRTEM) images indicate that hollow TiO_2 has the characteristic lattice plane of anatase TiO_2 (101), coated by Pd-HPP (Fig. 4b–d and Supplementary Fig. 15). The structure of Pd-HPP-TiO_2 was observed by TEM, and no Pd nanoparticle was detected in the HRTEM image, which is consistent with the XRD analysis. As further evidence, the elemental distributions were analyzed by scanning transmission electron microscopy (STEM) and energy-dispersive X-ray (EDX) mapping

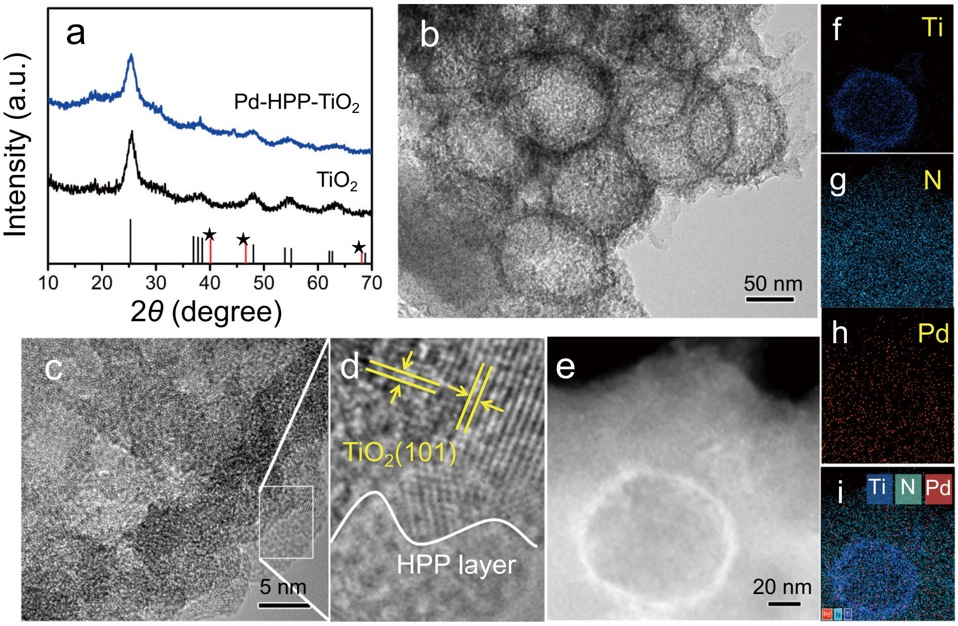

Fig. 4 Crystal and morphology characterizations. a XRD patterns of TiO_2 and Pd-HPP-TiO_2. The vertical lines are the position and intensity of anatase TiO_2 (JCPDS 21-1272) and Pd (labeled by the star, JCPDS 46-1043). **b** TEM, **c**, **d** HRTEM, **e** STEM, and **f**–**i** the corresponding EDX element mapping images of Pd-HPP-TiO_2.

tests. Figure 4e–i display that hollow TiO_2 is embedded in Pd-HPP with a homogeneous distribution of C, N, and Pd elements.

The chemical structure of Pd-HPP-TiO_2 was investigated by Fourier transform infrared (FT-IR) absorption, solid-state ^{13}C cross-polarization magic-angle spinning nuclear magnetic resonance (CP-MAS NMR), and X-ray photoelectron spectroscopy (XPS) measurements. As shown in FT-IR spectrum, the C-H stretching band at 2920–2960 cm^{-1} indicates the methylene linkage of HPP by solvent knitting (Supplementary Fig. 16)[46]. The broad bands of Ti-O-Ti stretching vibrations at 400–1000 cm^{-1} are observed for TiO_2 and Pd-HPP-TiO_2. The CP-MAS NMR spectrum of Pd-HPP-TiO_2 indicates evidence for the hyper-crosslinking process at the molecular level. The resonance peaks at 128, 137, and 146 ppm are attributed to the carbon atoms in the benzene ring and porphyrin ring (Fig. 5a). The peak with a chemical shift at 37 ppm corresponds to the methylene linkers, indicating the successful linking of TPP via the Friedel-Crafts reaction[47]. The chemical states of elements were analyzed by the XPS spectrum to display the presence of C, N, Ti, O, and Pd in the corresponding samples and the coexistence of them in Pd-HPP-TiO_2 (Supplementary Fig. 17). The high-resolution Pd 3*d* spectra in Fig. 5b show distinct doublet peaks at 343.3 and 338.1 eV, assigned to $3d_{5/2}$ and $3d_{3/2}$ of the coordinated Pd(II)[48,49]. In contrast, metallic Pd is predominantly observed in Pd/TiO_2 XPS, together with a weak shoulder peak of the adsorbed Pd^{2+} that remained without reducing[49,50]. Combined with the Pd-N signal in N 1*s* spectrum of Pd-HPP-TiO_2 (Supplementary Fig. 17), it is deduced that Pd coordinates successfully with the core of the porphyrin unit as Pd(II) but not as free Pd^{2+} or metallic Pd. The formation of Pd-HPP on hollow TiO_2 caused the binding energy of Ti 2*p* shifting to 0.7-eV higher energy (Supplementary Fig. 17). This shift reflects that the electron density of Ti is decreased by the electronic interaction with Pd-HPP, which is favorable for the electron transfer from TiO_2 to Pd-HPP during the photocatalytic reactions under UV-visible light irradiation.

Synchrotron-based X-ray absorption spectroscopy was employed to provide further information on the valence state. Figure 5c shows the Pd K-edge X-ray absorption near-edge structure (XANES) spectra. The absorption edge energy of Pd-HPP-TiO_2 is close to that of PdO but higher than that of Pd foil, confirming Pd(II) in Pd-HPP-TiO_2. Fourier transform of the extended X-ray absorption fine structure (EXAFS) displays the main peak at 1.5 Å for Pd-HPP-TiO_2 (Fig. 5d), arising from Pd-N bonding. No obvious peak was observed at the Pd-Pd position (2.5 Å) of Pd foil, indicating that Pd(II) sites were dispersed in Pd-HPP-TiO_2[48,51]. The structural parameters were obtained by the quantitative EXAFS curve fitting (Fig. 5e). Supplementary Table 6 reveals that the coordination number of Pd in Pd-HPP-TiO_2 is close to 4.0, indicating that Pd(II) coordinates to four N atoms of the porphyrin. The measured Pd-N bond distance of 2.03 Å is also close to the reported results of Pd-N_4 center[48,49]. Inductively coupled plasma mass spectrometry (ICP-MS) provides the accurate element composition, showing that the weight ratios of TiO_2 and Pd were 34.4% and 2.72%, respectively (Supplementary Table 7). Meanwhile, the similar Pd content was ensured in the control (Pd/TiO_2) to avoid the effect of metal amount on the photocatalytic activity. Based on the above characterizations, it is concluded that HPP is successfully formed on the surface of hollow TiO_2 and then Pd(II) coordinates to the porphyrin core of HPP to form Pd-HPP-TiO_2.

Photocatalytic mechanism of CO_2 reduction with H_2O. To clarify the reaction pathway, the reaction intermediates of CO_2 adsorption and photocatalytic reduction on the surface of Pd-HPP-TiO_2 were monitored by in-situ diffuse reflectance infrared Fourier transform spectra (DRIFTS). The spectra demonstrate the adsorption of CO_2 and H_2O on Pd-HPP-TiO_2 in the dark. The absorption band in the range of 3500–3800 cm^{-1} are in good agreement with those assigned to the stretching vibrations of surface-bonded OH groups and H_2O, suggesting the H_2O adsorption on the catalyst surface (Supplementary Fig. 18)[52,53]. The peaks at 1740, 1690, and 1640 cm^{-1} can be assigned to the surface adsorbed carbonate species (Fig. 5f)[54,55]. Under UV-visible light irradiation, the peaks at 1690 and 1640 cm^{-1} were significantly weakened. Meanwhile, the peak at 1740 cm^{-1} first became flat at 2 min and then changed to a negative peak with prolonged irradiation, which could be explained by the existence of pre-adsorbed carbonate species on the Pd-HPP-TiO_2 surface

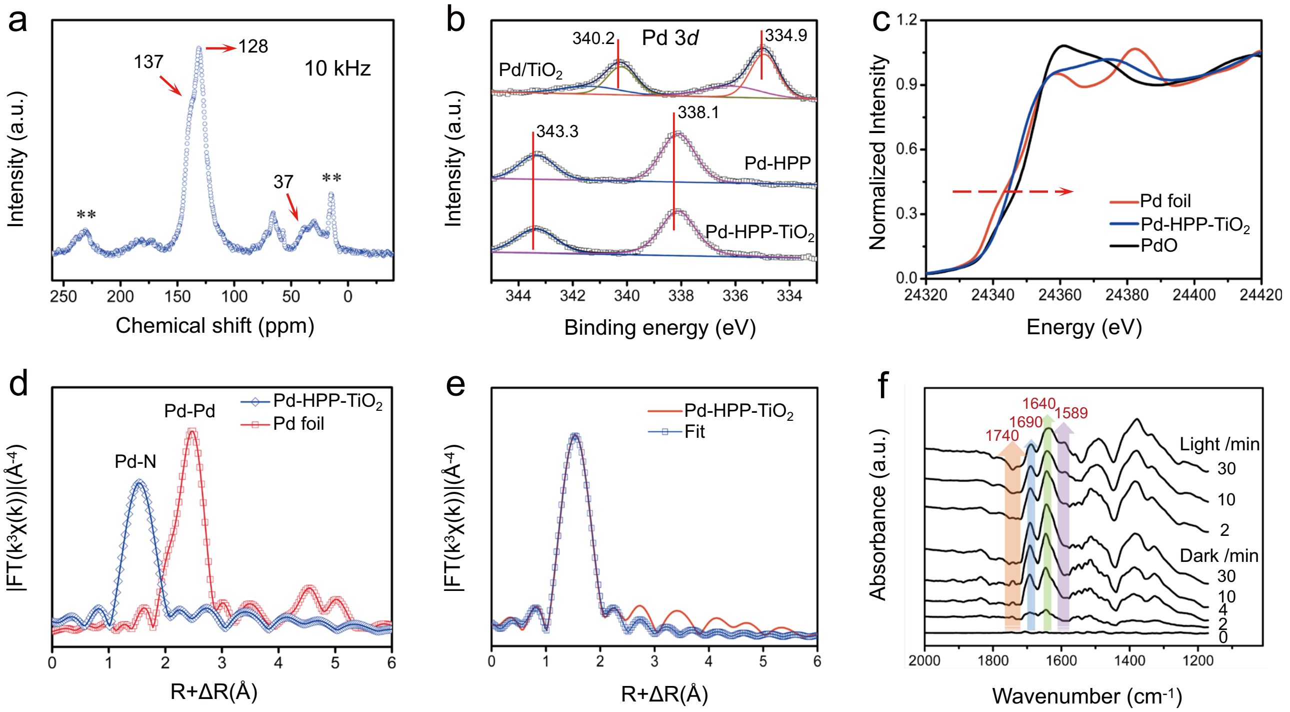

Fig. 5 Chemical structure analysis and surface species evolution of Pd-HPP-TiO$_2$. **a** Solid-state ^{13}C CP-MAS NMR spectrum. **b** Comparison of Pd 3*d* XPS spectra for three photocatalysts. **c** Pd K-edge XANES and **d** Fourier transformed EXAFS spectra of Pd-HPP-TiO$_2$ and references. **e** Fourier transformed EXAFS spectrum of Pd-HPP-TiO$_2$ and fitting curve. **f** In situ DRIFTS test of gas adsorption on Pd-HPP-TiO$_2$ in the dark and during the photocatalytic CO$_2$ reduction under UV-visible light irradiation.

before collecting the baseline due to its high CO$_2$ uptake. The results indicate the efficient consumption of surface carbonate during the photocatalytic reaction. Meanwhile, a new peak at 1589 cm^{-1} emerged in the spectra is suggested to be the C = O stretching vibration of *COOH groups, which was the vital intermediate for *CO formation and then transformed to CO and other fuels.[56–58] According to the detailed studies on the mechanism of CO$_2$ reduction, there are two possible pathways, i.e., one is the formaldehyde pathway and the other is the carbene pathway[59–61]. Although formaldehyde and methanol have been reported as products in some setups, they are not detected in this work. The photocatalytic CO$_2$ reduction in the gas-solid reaction can normally form CO and CH$_4$.[25,26] Therefore, the CO$_2$ reduction is more likely to be a carbene pathway as $CO_2 \rightarrow COOH \rightarrow CO \rightarrow \bullet C \rightarrow \bullet CH_3 \rightarrow CH_4$. The CO$_2$ molecules are activated at Pd(II) sites in Pd-HPP and then react with the proton and electron to produce the intermediate *COOH. Subsequent reaction with the electron and proton results in the splitting of *COOH into *CO and H$_2$O. At this time, part of CO is produced by *CO desorption. Since Pd can also function efficiently for the decomposition of H$_2$O to generate Pd-H species[62,63], the adsorbed *CO on Pd will be further react with the dissociated H to the formation of •C radicals, which can successively combine with •H radicals, thereby forming •CH, •CH$_2$, •CH$_3$, and finally CH$_4$ product[53,64–66].

The cycling experiment and related characterizations were carried out to investigate the photocatalytic sites of CH$_4$ evolution and the stability of Pd-HPP-TiO$_2$. As shown in Supplementary Fig. 19, Pd-HPP-TiO$_2$ showed about 80% of the initial photocatalytic activity for the CO$_2$ conversion after five consecutive cycles. The thermal stability of HPP is maintained up to 330 °C, as confirmed by thermogravimetric analysis (Supplementary Fig. 20). The comparison in FT-IR spectra of Pd-HPP-TiO$_2$ before and after the photocatalytic reaction reveals no obvious change in the chemical structure of Pd-HPP (Supplementary Fig. 21). A new peak at 40.1° is observed in the XRD pattern of Pd-HPP-TiO$_2$ after the cycling test to be assigned to Pd(0) (Supplementary Fig. 22), implying that a fraction of the coordinated Pd(II) was reduced to Pd(0) dissociating from the coordination sites to form Pd nanoparticles. XPS analysis in Supplementary Fig. 23a corroborates the reduction, leading to a decrease of the photocatalytic activity during the recycle. Such reduction suggests the electron trapped at Pd(II) for CO$_2$ reduction[67]. After five cycles, ~79% Pd existed as Pd(II) owing to the coordination to the porphyrin in microporous HPP, indicating the considerable stability of Pd-HPP-TiO$_2$ structure during the photocatalytic reaction. Pd nanoparticles are less active for the photocatalytic CO$_2$ reduction in air (Fig. 2e), compared to Pd(II) in Pd-HPP-TiO$_2$. Therefore, a tentative mechanism of photocatalytic CO$_2$ reduction over Pd-HPP-TiO$_2$ is proposed in Fig. 1. Benefiting from the high CO$_2$ adsorption capability and selectivity of HPP, CO$_2$ can be selectively enriched in Pd-HPP. Under UV light irradiation, the photogenerated electrons in the conduction band of TiO$_2$ transfer efficiently to Pd-HPP, the electrons are trapped at the coordinated Pd(II) in Pd-HPP, and the adsorbed CO$_2$ on Pd(II) is reduced to produce CH$_4$ and CO accompanied by the recovery of Pd(II), while the holes in the valence band of TiO$_2$ can oxidize water that adsorbed on hollow TiO$_2$ to produce O$_2$. The simultaneous monitoring of concentrations of CO$_2$ (decreased), CH$_4$, CO, and O$_2$ (produced), corroborates the overall redox reaction over Pd-HPP-TiO$_2$, applicable to aerobic environment, especially for flue gas with 3~5 vol% O$_2$ and air with 300~400 ppm of CO$_2$ and ~21 vol% O$_2$ content.

In summary, we have demonstrated that Pd-HPP-TiO$_2$, constructed based on higher CO$_2$ adsorption capability than O$_2$ and efficient charge separation for CO$_2$ reduction and H$_2$O oxidation, exhibits high photocatalytic activity for CO$_2$ reduction in an aerobic environment. In the presence of 5 vol% O$_2$, the CO$_2$ reduction over a catalyst without HPP (Pd/TiO$_2$) steeply drops to 6% of that in pure CO$_2$. In contrast, the O$_2$ inhibition is significantly less over Pd-HPP-

TiO_2, which maintained 46% of the CH_4 evolution rate in pure CO_2. Pd-HPP-TiO_2 shows the photocatalytic activity even in air with the CO_2 conversion yield of 12% and the CH_4 production of 24.3 μmol g^{-1} after 2 h UV-visible light irradiation, 4.5 times higher than those over Pd/TiO_2. The HPP layer effectively enriches CO_2 at Pd(II) to lessen the O_2 reduction. Water adsorbed on TiO_2 is oxidized by the holes in the valence band of TiO_2, leading to reduce the charge recombination and enhance CO_2 conversion. This study presents an insight into realizing the photocatalytic selective CO_2 reduction for effectively reducing CO_2 concentration in air or flue gas and producing valuable solar fuels as well.

Methods

Preparation of core-shell SiO_2@TiO_2 and hollow TiO_2 sphere. The preparation of SiO_2@TiO_2 was referenced in the literature[68]. In a 100 mL round bottom flask, a mixture containing 79 mL of ethanol, 3.9 mL of ammonia solution, and 1.4 mL of water was mixed with 1.0 g of SiO_2 nanoparticles with diameter of about 100 nm to obtain a SiO_2 colloidal solution. Then, 28 mL of acetonitrile was added to the above mixture with stirring at 4 °C. A solution containing 36 mL of ethanol, 12 mL of acetonitrile, and 1 mL of titanium isoporpoxide was added dropwise to the colloidal SiO_2 solution. The mixture was stirred vigorously for 12 h, and the resulting white solution was dried in an oven at 80 °C. After calcining the solution at 600 °C for 6 h, core-shell SiO_2@TiO_2 with diameter of 100–150 nm was obtained as a white powder. Hollow TiO_2 with thickness of about 10 nm were prepared by etching SiO_2@TiO_2 in 10 mL of 2.5 M NaOH solution for 2 days.

Preparation of Pd-HPP-TiO_2. HPP-TiO_2 was synthesized by an in-situ knitting method using SiO_2@TiO_2, 5,10,15,20-tetraphenylporphyrin (TPP), and dichloromethane (DCM, 8 mL) as a solid template, building block, and solvent, respectively. After uniform dispersion of SiO_2@TiO_2 and TPP in DCM, $AlCl_3$ catalyst was added at 0 °C with constant stirring. The reaction mixture was stirred at 0 °C for 4 h, 30 °C for 8 h, 40 °C for 12 h, 60 °C for 12 h, and 80 °C for 24 h under the protection of N_2 gas. Then, the sample was filtrated and washed twice with water and twice with ethanol, followed by further purification by extracting with ethanol for 2 days. Finally, the obtained solid was dried in a vacuum drying oven at 60 °C for 24 h, and etched in a 2.5 M NaOH solution for 2 days to yield HPP-TiO_2. 40 mg of HPP-TiO_2 or HPP was dispersed in 4 mL of acetonitrile and ultra-sounded for 5 min to obtain a homogeneous solution. Then 3 mL of H_2PdCl_4 solution (1.08 mg mL^{-1} Pd) was added and kept at 40 °C for 12 h. After the reaction stopped, the product was washed twice with water and twice with acetone, and vacuum dried at 60 °C overnight.

Preparation of Pd/TiO_2 as a reference. Pd nanoparticles were deposited on the surface of hollow TiO_2 from the photoreduction of Pd(II) on TiO_2: 100 mg of hollow TiO_2 was dispersed in 90 mL of deionized water and 10 mL of methanol. After ultrasonic treatment for 20 min, a certain amount of H_2PdCl_4 solution was added. Then, N_2 was continuously flowed into the solution for 20 min to ensure N_2-saturation. A mercury lamp was used for the photoreduction of H_2PdCl_4 on hollow TiO_2. After the photocatalytic reaction for 4 h, the solution was centrifuged and washed three times with ethanol and twice with water, and then dried overnight in a vacuum at 60 °C to yield Pd/TiO_2 as a gray powder.

Characterizations. Gas (N_2, CO_2, O_2) adsorption-desorption isotherms were analyzed by TriStar II 3flex adsorption apparatus (Micromeritics, USA). Samples were degassed at 100 °C for 12 h under vacuum before analysis. The structure and crystallinity of the samples were characterized using X-ray diffraction (XRD) analysis on an X-Pert PRO diffractometer with Cu-Kα radiation. The field emission scanning electron microscopy (FESEM) images were recorded by using a field emission scanning electron microscope (FEI Sirion 200, USA) at 10 kV. The high-resolution transmission electron microscopy (HR-TEM) and scanning transmission electron microscopy (STEM) images of samples were recorded on Tecnai G2 F30 microscope (FEI, Holland). The FT-IR experiment was conducted on a Bruker ALPHA Fourier transform infrared spectrometer. The Solid-state ^{13}C CP/MAS NMR spectra were tested on a WB 400 MHz Bruker Avance II spectrometer. The ^{13}C CP/MAS NMR spectra were collected on a 4 mm double resonance MAS probe at a rotation rate of 10 kHz. X-ray photoelectron spectroscopy (XPS) was measured with a monochromatic Mg Kα source on Thermo VG scientific ESCA MultiLab-2000, and the data were calibrated according to the C (carbon) 1 s peak (binding energy = 284.6 eV). The X-ray absorption spectra were collected on the beamline BL01C1 in NSRRC, and were provided technical support by Ceshigo Research Service "www.ceshigo.com". The radiation was monochromatized by a Si (111) double-crystal monochromator. XANES and EXAFS data reduction and analysis were processed by Athena software. The actual contents of Ti and different metals were measured by inductively coupled plasma mass spectrometry (NexION 300X, Perkin Elmer, USA). Photoluminescence (PL) emission spectra were collected by a Hitachi F-7000 spectrofluorometer at the excitation wavelength of 360 nm. UV-vis diffuse reflectance spectra (DRS) were obtained using a UV-vis spectrophotometer (UV-3600, Shimadzu, Japan). The reduction products from $^{13}CO_2$ were analyzed by HP 5973 gas chromatography-mass spectrometry (GC-MS). Thermogravimetric analysis (TGA) was carried out in N_2 and air from room temperature to 850 °C using the Perkin Elmer instrument Pyris1 TGA with a heating rate of 10 °C min^{-1}. The electrochemical and photoelectrochemical properties of the sample were tested using an electrochemical workstation (CHI650E, Chenhua Com., China) with a standard three-electrode system. A Pt wire and Ag/AgCl were used as the counter and reference electrodes, respectively. 5 mg of a catalyst was dispersed into 1 mL of 1:1 isopropanol/H_2O containing 10 μL of Nafion. Then, 50 μL of the above suspension was coated on an ITO glass as a working electrode. Electrochemical impedance spectra (EIS) were obtained in 0.1 M KCl electrolyte containing 5 mM $Fe(CN)_6^{3-}$/$Fe(CN)_6^{4-}$. Photocurrent signals were detected in 1 M Na_2SO_4 solution during light-on and light-off cycles.

Photocatalytic CO_2 reduction. 30 mg of powder sample was dispersed on the middle of the culture ware, placed in the sealed custom-made glass vessel, 10 cm away from the light source. The photocatalytic CO_2 reduction reaction was performed under 1 atm of a certain atmosphere (pure CO_2, CO_2/O_2 mixed gas, or air). 2 mL of water, as proton source for the CH_4 production, was dropped to the bottom of glass vessel and vaporized on standing. The reaction mixture was irradiated using a 300 W Xenon lamp (PLS-SXE300D, Beijing Perfectlight Technology, China) as light source. The full spectrum locates in the UV-visible light region (325~780 nm), as shown in Supplementary Fig. 24. For the visible light driven experiment, a cut-off filter of 420 nm was equipped with the lamp. The generated gases were analyzed by a gas chromatography analyzer (Shimadzu GC-2014C, Japan) with a flame ionization detector (FID) and an optic fiber oxygen sensor (Ocean-Optics, UK). The yield of CO_2 conversion was conducted in 0.2 vol% CO_2 in N_2 or air under irradiation for 4 h. To exclude the self-decomposition of samples, the sample was firstly irradiated for 4 h under N_2 to confirm the stability.

Data availability

The data supporting the findings of this study are available in the paper and Supplementary Information. Source data are provided with this paper.

Received: 9 April 2021; Accepted: 23 February 2022;

References

1. Tan, T. H. et al. Unlocking the potential of the formate pathway in the photo-assisted Sabatier reaction. *Nat. Catal.* **3**, 1034–1043 (2020).
2. Li, X., Yu, J., Jaroniec, M. & Chen, X. Cocatalysts for selective photoreduction of CO_2 into solar fuels. *Chem. Rev.* **119**, 3962–4179 (2019).
3. Jiang, Z. et al. Filling metal-organic framework mesopores with TiO_2 for CO_2 photoreduction. *Nature* **586**, 549–554 (2020).
4. Lu, K.-Q. et al. Rationally designed transition metal hydroxide nanosheet arrays on graphene for artificial CO_2 reduction. *Nat. Commun.* **11**, 5181 (2020).
5. Xu, F. et al. Unique S-scheme heterojunctions in self-assembled TiO_2/$CsPbBr_3$ hybrids for CO_2 photoreduction. *Nat. Commun.* **11**, 4613 (2020).
6. Wang, G. et al. Photoinduction of Cu single atoms decorated on UiO-66-NH_2 for enhanced photocatalytic reduction of CO_2 to liquid fuels. *J. Am. Chem. Soc.* **142**, 19339–19345 (2020).
7. Wu, H. et al. Metal-organic frameworks decorated cuprous oxide nanowires for long-lived charges applied in selective photocatalytic CO_2 reduction to CH_4. *Angew. Chem. Int. Ed.* **60**, 8455–8459 (2021).
8. Wang, S. et al. Porous hypercrosslinked polymer-TiO_2-graphene composite photocatalysts for visible-light-driven CO_2 conversion. *Nat. Commun.* **10**, 676 (2019).
9. Kanti, D. S., Piyali, B., Kundu, S. K., Saptarsi, M. & Asim, B. Role of surface phenolic-OH groups in N-rich porous organic polymers for enhancing the CO_2 uptake and CO_2/N_2 selectivity: experimental and computational studies. *ACS Appl. Mater. Interfaces* **10**, 23813–23824 (2018).
10. Alahmed, A. H., Briggs, M. E., Cooper, A. I. & Adams, D. J. Post-synthetic fluorination of scholl-coupled microporous polymers for increased CO_2 uptake and selectivity. *J. Mater. Chem. A* **7**, 549–557 (2019).
11. Comesaña-Gándara, B. et al. Redefining the robeson upper bounds for CO_2/CH_4 and CO_2/N_2 separations using a series of ultrapermeable benzotriptycene-based polymers of intrinsic microporosity. *Energy Environ. Sci.* **12**, 2733–2740 (2019).
12. Han, B. et al. Nickel metal-organic framework monolayers for photoreduction of diluted CO_2: metal-node-dependent activity and selectivity. *Angew. Chem. Int. Ed.* **57**, 16811–16815 (2018).
13. Wang, Y. et al. Hydroxide ligands cooperate with catalytic centers in metal-organic frameworks for efficient photocatalytic CO_2 reduction. *J. Am. Chem. Soc.* **140**, 38–41 (2018).
14. Zhong, W. et al. A covalent organic framework bearing single Ni sites as a synergistic photocatalyst for selective photoreduction of CO_2 to CO. *J. Am. Chem. Soc.* **141**, 7615–7621 (2019).

15. Wu, X. et al. Photocatalytic CO_2 conversion of $M_{0.33}WO_3$ directly from the air with high selectivity: insight into full spectrum-induced reaction mechanism. *J. Am. Chem. Soc.* **141**, 5267–5274 (2019).
16. Saito, D., Yamazaki, Y., Tamaki, Y. & Ishitani, O. Photocatalysis of a dinuclear Ru(II)-Re(I) complex for CO_2 reduction on a solid surface. *J. Am. Chem. Soc.* **142**, 19249–19258 (2020).
17. Dilla, M., Schlögl, R. & Strunk, J. Photocatalytic CO_2 reduction under continuous flow high-purity conditions: quantitative evaluation of CH_4 formation in the steady-state. *ChemCatChem* **9**, 696–704 (2017).
18. Yu, X. et al. Eosin Y-functionalized conjugated organic polymers for visible-light-driven CO_2 reduction with H_2O to CO with high efficiency. *Angew. Chem. Int. Ed.* **58**, 632–636 (2019).
19. Dilla, M., Jakubowski, A., Ristig, S., Strunk, J. & Schlogl, R. The fate of O_2 in photocatalytic CO_2 reduction on TiO_2 under conditions of highest purity. *Phys. Chem. Chem. Phys.* **21**, 15949–15957 (2019).
20. Lu, X. et al. A bio-inspired O_2-tolerant catalytic CO_2 reduction electrode. *Sci. Bull.* **64**, 1890–1895 (2019).
21. Wagner, A., Sahm, C. D. & Reisner, E. Towards molecular understanding of local chemical environment effects in electro- and photocatalytic CO_2 reduction. *Nat. Catal.* **3**, 775–786 (2020).
22. Kajiwara, T. et al. Photochemical reduction of low concentrations of CO_2 in a porous coordination polymer with a ruthenium (II)-CO complex. *Angew. Chem. Int. Ed.* **55**, 2697–2700 (2016).
23. Kang, S. & Lee, H. Recovery of CO_2 from flue gas using gas hydrate: thermodynamic verification through phase equilibrium measurements. *Environ. Sci. Technol.* **34**, 4397–4400 (2000).
24. Markewitz, P. et al. Worldwide innovations in the development of carbon capture technologies and the utilization of CO_2. *Energy Environ. Sci.* **5**, 7281–7305 (2012).
25. Li, H. et al. Selective visible-light-driven photocatalytic CO_2 reduction to CH_4 mediated by atomically thin $CuIn_5S_8$ layers. *Nat. Energy* **4**, 690–699 (2019).
26. Bian, J. et al. Dimension-matched Zinc phthalocyanine/$BiVO_4$ ultrathin nanocomposites for CO_2 reduction as efficient wide-visible-light-driven photocatalysts via a cascade charge transfer. *Angew. Chem. Int. Ed.* **58**, 10873–10878 (2019).
27. Blommaerts, N. et al. Tuning the turnover frequency and selectivity of photocatalytic CO_2 reduction to CO and methane using platinum and palladium nanoparticles on Ti-Beta zeolites. *Chem. Eng. J.* **410**, 128234 (2021).
28. Li, Y. et al. Facile top-down strategy for direct metal atomization and coordination achieving a high turnover number in CO_2 photoreduction. *J. Am. Chem. Soc.* **142**, 19259–19267 (2020).
29. Zheng, Z. et al. Correlation of the catalytic activity for oxidation taking place on various TiO_2 surfaces with surface OH-groups and surface oxygen vacancies. *Chem. Eur. J.* **16**, 1202–1211 (2010).
30. Corma, A. & Garcia, H. J. Photocatalytic reduction of CO_2 for fuel production: Possibilities and challenges. *J. Catal.* **308**, 168–175 (2013).
31. Mori, K., Yamashita, H. & Anpo, M. Photocatalytic reduction of CO_2 with H_2O on various titanium oxide Photocatalysts. *RSC Adv.* **2**, 3165–3172 (2012).
32. Kamat, P. V. & Jin, S. Semiconductor photocatalysis: “ tell us the complete story! *ACS Energy Lett.* **3**, 622–623 (2018).
33. Chang, X., Wang, T. & Gong, J. CO_2 photo-reduction: in-sights into CO_2 activation and reaction on surfaces of photocatalysts. *Energy Environ. Sci.* **9**, 2177–2196 (2016).
34. Anpo, M. et al. Applications of photoluminescence techniques to the characterization of solid surfaces in relation to adsorption, catalysis, and photocatalysis. *Adv. Catal.* **44**, 119–257 (1999).
35. Anpo, M. et al. Photoluminescence of zinc oxide powder as a probe of electron-hole surface processes. *J. Phys. Chem.* **88**, 5556–5560 (1984).
36. Anpo, M. et al. Photocatalytic reduction of CO_2 with H_2O on titanium oxides anchored within micropores of zeolites: effects of the structure of the active sites and the addition of Pt. *J. Phys. Chem. B* **101**, 2632–2636 (1997).
37. Lan, Z.-A. et al. Reducing the exciton binding energy of donor-acceptor based conjugated polymers to promote charge-induced reactions. *Angew. Chem. Int. Ed.* **58**, 10236–10240 (2019).
38. Schukraft, G. E. M. et al. Hypercrosslinked polymers as a photocatalytic platform for visible-light-driven CO_2 photoreduction using H_2O. *ChemSusChem* **14**, 1720–1727 (2021).
39. Zhang, H. et al. Isolated cobalt centers on $W_{18}O_{49}$ nanowires perform as a reaction switch for efficient CO_2 photoreduction. *J. Am. Chem. Soc.* **143**, 2173–2177 (2021).
40. Singh, G. et al. Emerging trends in porous materials for CO_2 capture and conversion. *Chem. Soc. Rev.* **49**, 4360–4404 (2020).
41. Xia, C., Wang, H., Kim, J. K. & Wang, J. Rational design of metal oxide-based heterostructure for efficient photocatalytic and photoelectrochemical systems. *Adv. Funct. Mater.* **31**, 2008247 (2021).
42. Thommes, M. et al. Physisorption of gases, with special reference to the evaluation of surface area and pore size distribution (IUPAC Technical Report). *Pure Appl. Chem.* **87**, 1051–1069 (2015).
43. Graham, C., Pierrus, J. & Raab, R. E. Measurement of the electric quadrupole moments of CO_2, CO and N_2. *Mol. Phys.* **67**, 939–955 (1989).
44. Couling, V. W. & Ntombela, S. S. The electric quadrupole moment of O_2. *Chem. Phys. Lett.* **614**, 41–44 (2014).
45. Chen, L., Cao, F. & Sun, H. Ab initio study of the π-π interactions between CO_2 and benzene, pyridine, and pyrrole. *Int. J. Quantum Chem.* **113**, 2261–2266 (2013).
46. Wang, S. et al. Layered microporous polymers by solvent knitting method. *Sci. Adv.* **3**, 1602610 (2017).
47. Wang, S. et al. A novel metalporphyrin-based microporous organic polymer with high CO_2 uptake and efficient chemical conversion of CO_2 under ambient conditions. *J. Mater. Chem. A* **5**, 1509–1515 (2017).
48. He, Q. et al. Accelerating CO_2 electroreduction to CO over Pd single-atom catalyst. *Adv. Funct. Mater.* **30**, 2000407 (2020).
49. Zhou, S. et al. Pd single-atom catalysts on nitrogen-doped graphene for the highly selective photothermal hydrogenation of acetylene to ethylene. *Adv. Mater.* **31**, 1900509 (2019).
50. Selishchev, D. S. et al. Deposition of Pd nanoparticles on TiO_2 using a $Pd(acac)_2$ precursor for photocatalytic oxidation of CO under UV-LED irradiation. *Appl. Catal. B-Environ.* **235**, 214–224 (2018).
51. Yan, H. et al. Single-atom Pd1/Graphene catalyst achieved by atomic layer deposition: remarkable performance in selective hydrogenation of 1,3-Butadiene. *J. Am. Chem. Soc.* **137**, 10484–10487 (2015).
52. Long, R. et al. Isolation of Cu atoms in Pd lattice: forming highly selective sites for photocatalytic conversion of CO_2 to CH_4. *J. Am. Chem. Soc.* **139**, 4486–4492 (2017).
53. Neațu, Ş., Maciá-Agulló, J. A., Concepción, P. & Garcia, H. Gold-copper nanoalloys supported on TiO_2 as photocatalysts for CO_2 reduction by water. *J. Am. Chem. Soc.* **136**, 15969–15976 (2014).
54. Zhang, H. et al. An unprecedent hydride transfer pathway for selective photocatalytic reduction of CO_2 to formic acid on TiO_2. *Appl. Catal. B-Environ.* **284**, 119692 (2021).
55. Sheng, J. et al. Identification of halogen-associated active sites on bismuth-based perovskite quantum dots for efficient and selective CO_2-to-CO photoreduction. *ACS Nano* **14**, 13103–13114 (2020).
56. Zhu, J. et al. Asymmetric triple-atom sites confined in ternary oxide enabling selective CO_2 photothermal reduction to acetate. *J. Am. Chem. Soc.* **143**, 18233–18241 (2021).
57. Di, J. et al. Surface local polarization induced by bismuth-oxygen vacancy pairs tuning non-covalent interaction for CO_2 photoreduction. *Adv. Energy Mater.* **11**, 2102389 (2021).
58. Wang, S. et al. Intermolecular cascaded π-conjugation channels for electron delivery powering CO_2 photoreduction. *Nat. Commun.* **11**, 1149 (2020).
59. Rawool, S. A. et al. Defective TiO_2 for photocatalytic CO_2 conversion to fuels and chemicals. *Chem. Sci.* **12**, 4267 (2021).
60. Habisreutinger, S. N. et al. Photocatalytic reduction of CO_2 on TiO_2 and other semiconductors. *Angew. Chem. Int. Ed.* **52**, 7372–7408 (2013).
61. Ji, Y. F. et al. Theoretical study on the mechanism of photoreduction of CO_2 to CH_4 on the anatase TiO_2 (101) surface. *ACS Catal.* **6**, 2018–2025 (2016).
62. Gao, D. et al. Pd-containing nanostructures for electrochemical CO_2 reduction reaction. *ACS Catal.* **8**, 1510–1519 (2018).
63. Fan, Z. et al. Synthesis of 4H/fcc noble multimetallic nanoribbons for electrocatalytic hydrogen evolution reaction. *J. Am. Chem. Soc.* **138**, 1414 (2016).
64. Anpo, M. et al. Photocatalytic reduction of CO_2 with H_2O on various titanium oxide catalysts. *J. Electroanal. Chem.* **396**, 21–26 (1995).
65. Fan, J. et al. Insight into synergetic mechanism of Au@Pd and oxygen vacancy sites for coupling light-driven H_2O oxidation and CO_2 reduction. *J. Catal.* **378**, 164–175 (2019).
66. Liu, J. et al. Mechanism of CO_2 photocatalytic reduction to methane and methanol on defected anatase TiO_2 (101): A DFT study. *J. Phys. Chem. C.* **123**, 3505–3511 (2019).
67. Han, N. et al. Supported cobalt polyphthalocyanine for high-performance electrocatalytic CO_2 reduction. *Chem* **3**, 652–664 (2017).
68. Son, S., Hwang, S. H., Kim, C., Yun, J. & Jang, J. Designed synthesis of SiO_2/TiO_2 core/shell structure as light scattering material for highly efficient dye-sensitized solar cells. *ACS Appl. Mater. Interfaces* **5**, 4815–4820 (2013).

Acknowledgements

This work was financially supported by the National Natural Science Foundation of China (22122602, 21771070, 22161142005) and the Fundamental Research Funds for the Central Universities (2019KFYRCPY104, 2018KFYYXJJ120). We thank the Analysis and Testing Center, Huazhong University of Science and Technology for the characterization of materials.

Author contributions

J.W. conceived the project and designed the experiments. Y.M. and X.Y. performed the experiments and analyzed the data. S.W. helped the synthesis. T.L. and B.T. discussed the

results. C.C. designed the photocatalytic tests. B.T., C.C., T.M., E.R.W. and H.Z. helped in improving the manuscript. Y.M., J.W., and H.Z. co-wrote the manuscript.

Materials availability

Correspondence and requests for materials should be addressed to J.W

Competing interests

The authors declare no competing interests.

Additional information

Supplementary information The online version contains supplementary material available at https://doi.org/10.1038/s41467-022-29102-0.

Correspondence and requests for materials should be addressed to Jingyu Wang.

Peer review information *Nature Communications* thanks Masakazu Anpo and the other, anonymous, reviewer(s) for their contribution to the peer review of this work. Peer reviewer reports are available.